The Boreal Summer Intraseasonal Oscillation Simulated in the NCEP Climate Forecast System: The Effect of Sea Surface Temperature

KYONG-HWAN SEO*

RS Information Systems, McLean, Virginia, and NOAA/NCEP/Climate Prediction Center, Camp Springs, Maryland

JAE-KYUNG E. SCHEMM, WANQIU WANG, AND ARUN KUMAR

NOAA/NCEP/Climate Prediction Center, Camp Springs, Maryland

(Manuscript received 16 May 2006, in final form 3 August 2006)

ABSTRACT

Observational evidence has indicated the important role of the interaction of the atmosphere with the sea surface in the development and maintenance of the tropical intraseasonal oscillation (ISO). However, improvements in ISO simulations with fully coupled atmosphere–ocean general circulation models are limited and model dependent. This study further examines the effect of air–sea coupling and the basic-state sea surface temperature (SST) associated with the boreal summer intraseasonal oscillation (BSISO) in a 21-yr free run with the recently developed NCEP coupled Climate Forecast System (CFS) model. For this, the CFS run is compared with an Atmospheric Model Intercomparison Project–type long-term simulation forced by prescribed SST in the NCEP Global Forecast System (GFS) model and flux-corrected version of CFS (referred to as CFSA). The GFS run simulates significantly unorganized BSISO convection anomalies, which exhibit an erroneous standing oscillation. The CFS run with interactive air–sea coupling has limited improvements, including the generation of intraseasonal SST variation preceding the convection anomaly by ~10 days. However, this simulation still does not show the observed continuous northward propagation over the Indian Ocean due to a cold model bias. The CFSA run removes the cold bias in the Indian Ocean and the simulation of the development and propagation of BSISO anomalies are significantly improved. Enhanced and suppressed convection anomalies exhibit the observed quadrupole-like configuration, and phase relationships between precipitation and surface dynamic and thermodynamic variables for the northward propagation are shown to be coherent and consistent with the observations. It is shown that the surface meridional moisture convergence is an important factor for the northward propagation of the BSISO. On the other hand, both the GFS and CFS runs do not realistically simulate an eastward-propagating equatorial mode. The CFSA run produces a more realistic eastward-propagation mode only over the Indian Ocean and Java Sea due to the improved mean state in SST, low-level winds, and vertical wind shear. Reasons for the failure of farther eastward propagation into the west Pacific in CFSA are discussed. This study reconfirms the significance of air–sea interactions. More importantly, however, the results suggest that in order for the influence of the coupled air–sea interaction to be properly communicated, the mean state SST in the coupled model should be reasonably simulated. This is because the basic-state SST itself acts to sustain BSISO convection and it makes the large-scale dynamical environment (i.e., easterly vertical wind shear or low-level westerly zonal wind) more favorable for the propagation of the moist Rossby–Kelvin wave packet.

1. Introduction

The propagation characteristic of the tropical intraseasonal oscillation (ISO) undergoes a peculiar seasonal variation. The boreal winter and springtime intraseasonal oscillation, known as the Madden–Julian oscillation (MJO), is characterized by dipole convective anomalies in the warm pool with a pronounced eastward propagation (e.g., Madden and Julian 1994; Hendon and Salby 1994, 1996; Seo and Kim 2003; Sperber 2003; Wheeler and Hendon 2004), whereas the boreal summertime intraseasonal oscillation (BSISO) has a complex spatial structure and propagation pattern due to the northward migration of the thermal equator and the interaction with the Asian summer monsoon (e.g., Lau and Chan 1986; Annamalai and Slingo 2001;

* Current affiliation: Division of Earth Environmental System, Atmospheric Science Major, Pusan National University, Busan, South Korea.

Corresponding author address: Dr. Kyong-Hwan Seo, Dept. of Atmospheric Sciences, Pusan National University, Busan 609-734, South Korea.
E-mail: khseo@pusan.ac.kr

DOI: 10.1175/MWR3369.1

Kemball-Cook and Wang 2001). For the BSISO, eastward-propagating convection anomalies along the equator coexist with northward-propagating convection anomalies from the Indian Ocean to the Indian subcontinent, and also with the northwestward-moving anomalies in the western Pacific (e.g., Lau and Chan 1986; Annamalai and Slingo 2001; Hsu and Weng 2001; Kemball-Cook and Wang 2001; Lawrence and Webster 2001; Jones et al. 2004; Seo et al. 2005).

The propagation features of the BSISO have pronounced regional influences, for example, the life cycle of the Asian summer monsoon system. The intraseasonal tropical convection variation over the Indian Ocean and the South China Sea is connected to the onset and retreat of the Indian summer monsoon and the rainy spells over China (mei-yu; Sikka and Gadgil 1980; Lau and Chan 1986; Annamalai and Slingo 2001). The active and break spells of the monsoon are due to the northward propagation of the convective anomaly from the Bay of Bengal or the Indian Ocean over to the Indian subcontinent (Krishnan et al. 2000; Annamalai and Slingo 2001). Interaction between diabatic heating associated with the BSISO and large-scale circulation also affects remote regions via teleconnection. For example, the BSISO modulates the summertime intraseasonal precipitation variability in the extratropical region (Kawamura et al. 1996; Mo 2000). Also, the BSISO occurring in the eastern Pacific Ocean has been demonstrated to change sea surface temperature (SST) and modulate tropical cyclone activity (Maloney and Hartmann 2000; Maloney and Kiehl 2002). Furthermore, there exists clear evidence that a proper representation of tropical intraseasonal convective forcing in atmospheric models helps enhance extended-range weather forecast skill in the extratropics (Ferranti et al. 1990).

To understand the major factors responsible for the observed characteristics of the BSISO, the role of SST and air–sea coupling on the ISO has received growing interest. Krishnamurti et al. (1988) demonstrated evidence of SST fluctuations in relation to the ISO over the tropical Indian Ocean and western Pacific. A theoretical study by Wang and Xie (1998) showed the importance of the ocean mixed layer thermodynamics in destabilizing the MJO and a selection mechanism that favors the growth of planetary-scale waves. Diagnostic analyses by many authors (Zhang 1996; Shinoda et al. 1998; Woolnough et al. 2000; Hsu and Weng 2001; Kemball-Cook and Wang 2001, among others) have provided significant evidence of coupled air–sea interaction in the maintenance and development of the boreal winter MJO and boreal summer ISO.

In contrast to the observational and theoretical analysis, however, various studies with general circulation models (Flatau et al. 1997; Waliser et al. 1999; Hendon 2000; Kemball-Cook et al. 2002; Inness and Slingo 2003; Inness et al. 2003; Fu et al. 2003; Fu and Wang 2004; Sperber 2004) suggested that the inclusion of coupled air–sea interactions does not always lead to improvements in the model-simulated ISO. Some model studies show that the coupled air–sea interaction improves the eastward propagation of the boreal winter MJO and northward propagation of the boreal summer ISO, as well as simulation of their intensity and period. Improvements tend to occur when coupled models are capable of simulating observed relationships among convection, surface heat fluxes, and SST associated with the ISO, and in such cases the ISO in the coupled model simulations are indeed improved compared with the simulations in the atmosphere-only integrations. But when models failed to capture the observed relationship between convection and surface heat flux due to a certain deficiency, such as erroneous mean surface winds and SST (Hendon 2000; Inness and Slingo 2003), the simulated ISO was not improved by the inclusion of coupled air–sea interaction. So in this paper, the role of coupled air–sea interaction on the characteristics of BSISO is further studied using the coupled model at the National Centers for Environmental Prediction (NCEP).

A new operational global atmosphere–ocean coupled Climate Forecast System (CFS) model has been recently implemented at NCEP for seasonal climate prediction (Saha et al. 2006; Wang et al. 2005). The CFS model is composed of the recent version of the NCEP atmospheric model and the Geophysical Fluid Dynamics Laboratory (GFDL) oceanic model. A preliminary result on the ENSO-related interannual variability in the CFS model has been reported in Wang et al. (2005) and various other studies on atmospheric and ocean variability including teleconnection, Asian summer monsoon, oceanic Kelvin wave variability, and their skill score evaluation are currently under way.

The focus of this study is the role of coupled air–sea interactions on the northward and eastward propagation, and the coherent relationships among BSISO convection and associated dynamic and thermodynamic variables. Analysis includes a comparison of a long coupled CFS control simulation with a simulation from an atmosphere-only version of the CFS. As long simulations of coupled models also generate SST biases that could adversely influence the characteristics of BSISO, an additional surface flux-corrected coupled run is also performed to evaluate if the development and propa-

gation of BSISO signals can be further improved by reduced SST biases. Of practical relevance, we also present evidence that the real-time forecasts from the CFS have improved the BSISO signal compared to the corresponding uncoupled GFS forecast.

Section 2 describes the models, simulation configurations, and the methods to diagnose the results. Seasonal mean climatologies as well as the intraseasonal variability of tropical precipitation of the uncoupled and coupled simulation runs are presented in section 3. In section 4, we examine the phase relationships among convection, surface heat flux, surface temperature, and surface dynamic variables associated with the BSISO. Section 5 describes the effect of the basic-state SST on the development and propagation of BSISO modes from the flux-corrected CFS simulation. In section 6 summary and discussions are given and the first evidence of the forecast skill difference between the NCEP uncoupled and coupled models is presented.

2. The models and simulations

a. The models

The atmospheric component of the coupled CFS is a version of the NCEP Global Forecast System (GFS) model as of February 2003. It adopts a spectral truncation of 62 waves (T62) in the horizontal and 64 sigma layers in the vertical. The oceanic component is the GFDL Modular Ocean Model version 3 (MOM3; Pacanowski and Griffies 1998). The spatial domain for MOM3 in CFS is quasiglobal, extending from 74°S to 64°N. The zonal resolution is 1°. The meridional resolution is 1/3° between 10°S and 10°N, linearly increasing to 1° poleward of 30°S and 30°N. There are 40 layers in the vertical with 27 layers in the upper 400 m. The atmospheric and oceanic components are coupled once per day. Sea ice extent is prescribed from the observed climatology. An upgraded version of the simplified Arakawa–Schubert scheme (Pan and Wu 1995) by Hong and Pan (1998) is used for cumulus convection parameterization. More details of the CFS model can be found in Saha et al. (2006).

b. The simulations and observations

Analysis in this study is based on an atmosphere-only Atmospheric Model Intercomparison Project (AMIP)-type simulation with the atmospheric component of the CFS (i.e., the GFS), a Coupled Model Intercomparison Project (CMIP)-type simulation with the CFS, and the flux-adjusted CMIP simulation with the CFS. The AMIP-type simulation with the GFS was forced with observed monthly mean SST from 1982 to 2002. The prescribed SST was taken from the weekly analysis of Reynolds et al. (2002). This run is referred to as the GFS run or GFS briefly. Note that it is more appropriate to use the monthly mean SSTs as a boundary forcing than the weekly or daily SSTs because the high-frequency variability in the observed SST contains signature of fully coupled air–sea interactions and when specified in the AMIP simulations, it interferes with the internal atmospheric dynamics and variability on a similar time scale. Indeed, this point is well illustrated in Fu and Wang (2004) and Zheng et al. (2004) where an atmosphere-only simulation forced by daily SST produces erroneous intraseasonal variations and an unrealistic phase relationship between convection and SST.

Several CMIP multidecade control simulations have been performed with the CFS, and have been diagnosed to investigate the model's capability in simulating interannual variability (Wang et al. 2005). In this study, a 21-yr segment from one of the CFS simulations is used. This simulation was initialized from observed analyses of 1 January 2002. The initial condition for the atmosphere was taken from the NCEP Department of Energy (DOE) Reanalysis-2 (R2; Kanamitsu et al. 2002) and the initial condition for the ocean was from an NCEP global ocean data assimilation system (GODAS; Behringer and Xue 2004; Seo and Xue 2005). This simulation is referred to as the CFS.

While the CFS includes the coupled air–sea interaction (the importance of which will be shown in the representation of the ISO) biases in air–sea interaction also inevitably induce errors in the simulated SSTs, which may also adversely affect the simulated ISO. The amplitude of the tropical annual-mean SST bias in the CFS run can be as large as 2 K. To reduce SST biases, and at the same time to maintain coupled air–sea interactions, another simulation with the CFS, but with a flux adjustment to the ocean surface flux components, is also analyzed. This simulation is referred to as the CFSA. The flux adjustment for CFSA was taken as the differences between fluxes produced from the AMIP simulation with GFS using observed SSTs and fluxes used to drive uncoupled MOM3, which produced SSTs that are close to the observations. Momentum fluxes for the uncoupled MOM3 are taken from R2. Heat and freshwater fluxes for the uncoupled MOM3 are taken from the fluxes from R2 plus additional values. These additional values for heat and freshwater fluxes were calculated by forcing MOM3 with R2 ocean surface fluxes and with relaxation terms for SST and sea surface salinity (SSS) with a time scale of 10 days. These relaxation terms for SST and SSS are saved and added to the R2 fluxes to form the total fluxes for the un-

coupled MOM3. As will be demonstrated, the CFSA has less bias in seasonal mean SST, wind, and vertical shear in the Indian Ocean, leading to the most improved simulation of the northward-propagating mode.

Observational datasets used in this study include daily NCEP DOE R2 (Kanamitsu et al. 2002) and daily precipitation interpolated from the pentad Climate Prediction Center (CPC) Merged Analysis of Precipitation (CMAP; Xie and Arkin 1997). Calculations for intraseasonal variability are based on 20–100-day bandpass-filtered time series using a Lanczos filter (Duchon 1979) for the months of June–September (JJAS).

c. Methods of analysis

To extract the evolving pattern of the BSISO, an extended EOF analysis (EEOF) is applied to the intraseasonally filtered precipitation anomalies during JJAS for the observation and three simulation runs, separately. In the EEOF analysis, a window of 50 days is used to capture a dominant BSISO signal (see also Lau and Chan 1986). Other key variables (e.g., large-scale circulation, surface heat flux, surface temperature, surface moisture convergence, and surface vorticity) are regressed against the EEOF principal components to provide a consistent picture of circulation and surface variability associated with BSISO convection. Variations in the applied window width do not show any significant change in the result. Also, the EEOF and corresponding regression analyses based on outgoing longwave radiation (OLR), which provides a more continuous proxy data for convection than precipitation, lead to virtually identical conclusions.

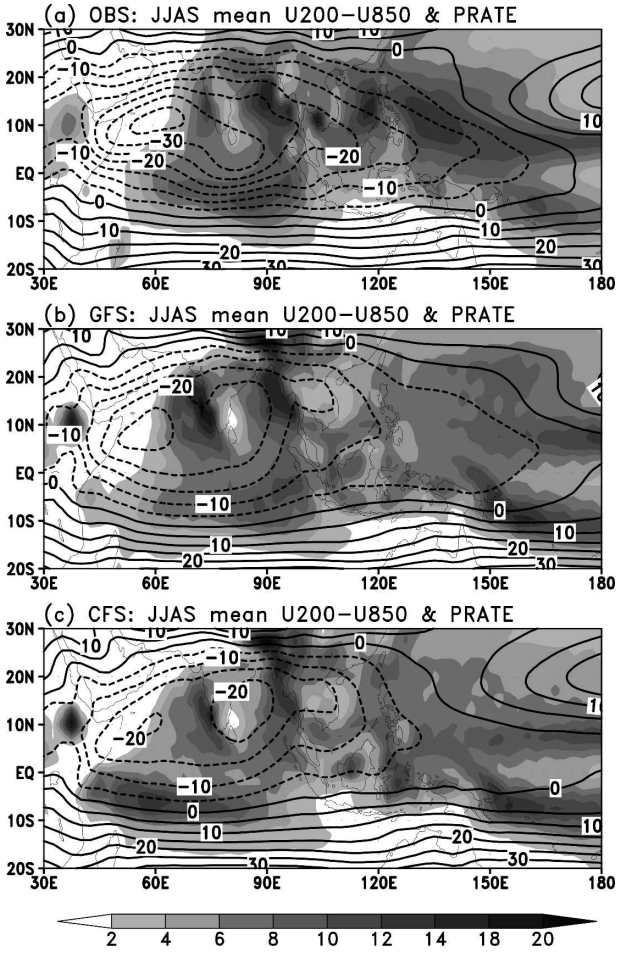

FIG. 1. JJAS mean precipitation rate (mm day^{-1}, shaded) and vertical shear of zonal winds (U200–U850, contours) for (a) the observations (CMAP precipitation rate and winds from the NCEP R2), (b) the GFS run, and (c) the CFS run. The contour interval is 5 m s^{-1}.

3. Seasonal mean state and intraseasonal variability

a. Rainfall and vertical wind shear

In this section, we will first describe some aspects of the seasonal mean climatology that may impact intraseasonal variability. Figure 1 compares precipitation rate and vertical shear of zonal winds between the observations and simulations in boreal summer (defined as JJAS). Both simulations produce double rainbelts near the equator and along 15°N. However, the large rainfall area in the Indian Ocean (south of the equator) in CFS is centered ~30° to the west of the observed one. Also, the rainfall in the eastern Arabian Sea and Bay of Bengal is overestimated in the GFS run (Fig. 1b), but is slightly more realistic in the CFS run (Fig. 1c). The rainfall in the South China Sea and the western North Pacific (WNP) in both simulations is not well simulated, and further, the models tend to generate a spurious double intertropical convergence zone (ITCZ) in the west Pacific (Figs. 1b,c) instead of a dominant northern ITCZ as in the observation (Fig. 1a).

The vertical shear in the mean zonal wind is shown to be very critical for both the northward propagation and eastward propagation along the equator (Zhang and Geller 1994; Wang and Xie 1997; Kemball-Cook et al. 2002). The easterly vertical wind shear favors the emission of Rossby waves, as well as the eastward-propagating equatorial waves by diabatic heating associated with the ISO. The model simulations capture the observed overall pattern with easterly shear northward of 10°S over the Indian Ocean and western Pacific, but the shear in both models is weaker than the observation. The CFS model moderately reproduces the large-scale circulation and rainfall features associated with the Asian (especially Indian) summer monsoon.

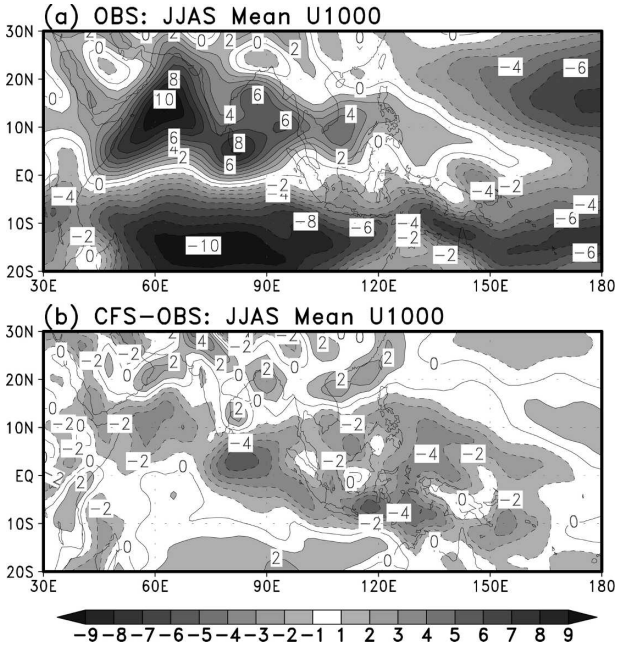

FIG. 2. JJAS mean 1000-hPa zonal winds ($m\,s^{-1}$) for (a) the observation, (b) the CFS run, and (c) the difference between the CFS run and the observation. The contour interval is 1 $m\,s^{-1}$.

b. 1000-hPa zonal winds

The realistic simulation of mean surface zonal winds is also an important factor for the reasonable representation of surface latent heat flux (e.g., Hendon 2000; Inness and Slingo 2003). The surface latent heat flux acts to regulate intraseasonal SST oscillation, which in turn provides favorable condition for surface moisture convergence and atmospheric instability. Figure 2 presents observed JJAS mean 1000-hPa zonal winds and difference between the observation and the CFS simulation. The GFS surface zonal winds are not shown since SST is not calculated from the simulated surface heat fluxes but specified as observed. In fact, the zonal winds in the GFS simulation are similar to the observed. The observed westerlies over the regions of the Asian summer monsoon and the BSISO (Fig. 2a) are captured by CFS but with weaker amplitude over the northern Indian Ocean (Fig. 2b). Especially, easterly bias appears over the eastern Indian Ocean, near Indonesia (0°, 95°–105°E) and the region extending from the Philippine Islands (10°N, 110°–130°E) to the WNP. As will be discussed later, the easterly bias in these regions in the CFS run is related to SST errors.

c. Sea surface temperature

Simulated SST errors in the CFS simulation are shown in Fig. 3. Except for a warm bias with a magnitude of 1.5 K over the western Indian Ocean, cold bias dominates over the central and eastern Indian Ocean, the Java Sea, near the Maritime Continent, and in the west Pacific. The cold bias over the equatorial eastern Indian Ocean is generally located south of the equator, where the stronger easterly zonal wind anomaly than that of the observation appears (Fig. 2b). The increased total wind speed due to the easterly anomaly induces stronger evaporation and cold SST bias develops. Also, the decreased seasonal mean precipitation amount (Fig. 1b) is related to this cold bias. Similarly, the cold bias along the western portion of the ITCZ in the WNP in CFS represents significantly reduced mean convective activity in this area (Fig. 1c).

d. Intraseasonal variability of rainfall

Figure 4 shows the standard deviation of tropical intraseasonal (20–100 day) rainfall in JJAS for the observation and the GFS and the CFS runs. For the observed

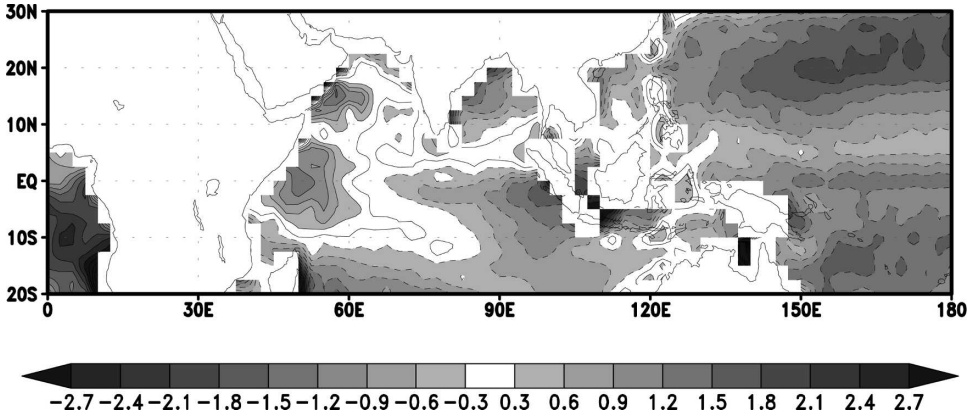

FIG. 3. JJAS mean SST difference (K) between the CFS run and the observation. The contour interval is 0.5 K.

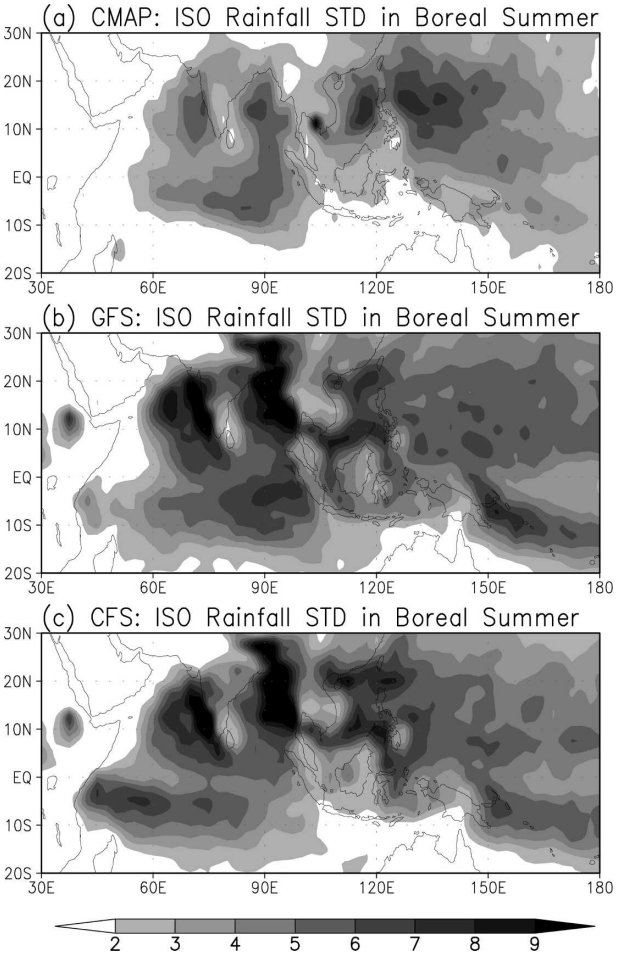

FIG. 4. JJAS mean standard deviation of intraseasonal precipitation rate (mm day^{-1}, shaded) for (a) the observation (CMAP rainfall), (b) the GFS run, and (c) the CFS run.

field, five regions with local maximum in rainfall are identified as in Fu and Wang (2004): the eastern Arabian Sea, the Bay of Bengal, the South China Sea, the WNP, and the equatorial Indian Ocean. The off-equatorial peaks are due to deep convection that propagates northward sequentially along the regions listed above (see Fig. 5). Both GFS and CFS capture the overall observed pattern, but rainfall variability in the eastern Arabian Sea and Bay of Bengal is stronger than that in the observation. The equatorial Indian Ocean rainfall maximum in CFS is shifted ~30° west to the observed one, as in the shift in the seasonal mean state. Rainfall variability over the WNP and South China Sea is simulated slightly better in CFS than in GFS. Finally, both GFS and CFS exhibit considerably stronger intraseasonal variability in the western Pacific south of the equator in association with the erroneous southern ITCZ as shown in seasonal mean precipitation (Fig. 1).

4. Simulation of the northward-propagating signal and the eastward-moving equatorial mode

a. Life cycle of the BSISO convection

The life cycle of the BSISO is identified based on the EEOF analysis. This is conducted over the global Tropics (30°S–30°N, 0°–360°E). According to North et al.'s (1982) rule of thumb, the first two modes of the EEOF analysis for JJAS CMAP precipitation are identified to be significantly different from the higher modes. These two modes account for about 9.3% of total daily rainfall variability and represent the prominent evolution pattern of the BSISO with a quarter-cycle phase difference (~10–12 days) between the two principal components. This 90° out-of-phase relationship is due to the nonstationary nature of the ISO (Seo and Kim 2003). Figure 5 shows the first mode of CMAP precipitation for JJAS with each panel 4 days apart and illustrating a typical life cycle of the BSISO with a period of ~40–45 days. The initiation of the cycle is marked by enhancement of the convection in the equatorial Indian Ocean (t = 1). This convection anomaly strengthens and moves eastward with time. Over the Indian Ocean, the convection anomaly elongates to the north and south as Rossby waves are emitted (t = 13–17). The northern lobe propagates steadily northward, while the southern one is diminished by t = 25. A Kelvin wave response extends toward the date line. This northern lobe of the Rossby waves and the eastward-moving convective anomaly from the Kelvin waves form a diagonally elongated convective band. Along with these, the suppressed convection of the previous cycle in the South China Sea and the new suppressed convection in the equatorial Indian Ocean exhibit a quadrupole-like configuration (t = 25–29). This pattern suggests that the Indian monsoon generally exhibits an opposite phase variation with the China monsoon (Krishnan et al. 2000). By the time when the northward-moving precipitation anomaly decays over the foothills of the Himalayas (t = 33–37), possibly due to the surface friction and decreased moisture supply, suppressed convection in the equatorial Indian Ocean is well developed and begins to emit the northern and southern Rossby waves. The convection anomalies developed near the Maritime Continent and western Pacific (t = 17–21) propagate northward (t = 25–37 and t = 1) and subsequently weaken near the southeastern China continent (t = 5–9). From the life cycle, it is seen that separate enhanced convection anomalies propagate northward or northwestward in a sequential order from the west to the east: first, the eastern Arabian Sea (70°E), next the Bay of Bengal (90°E), then the South China Sea

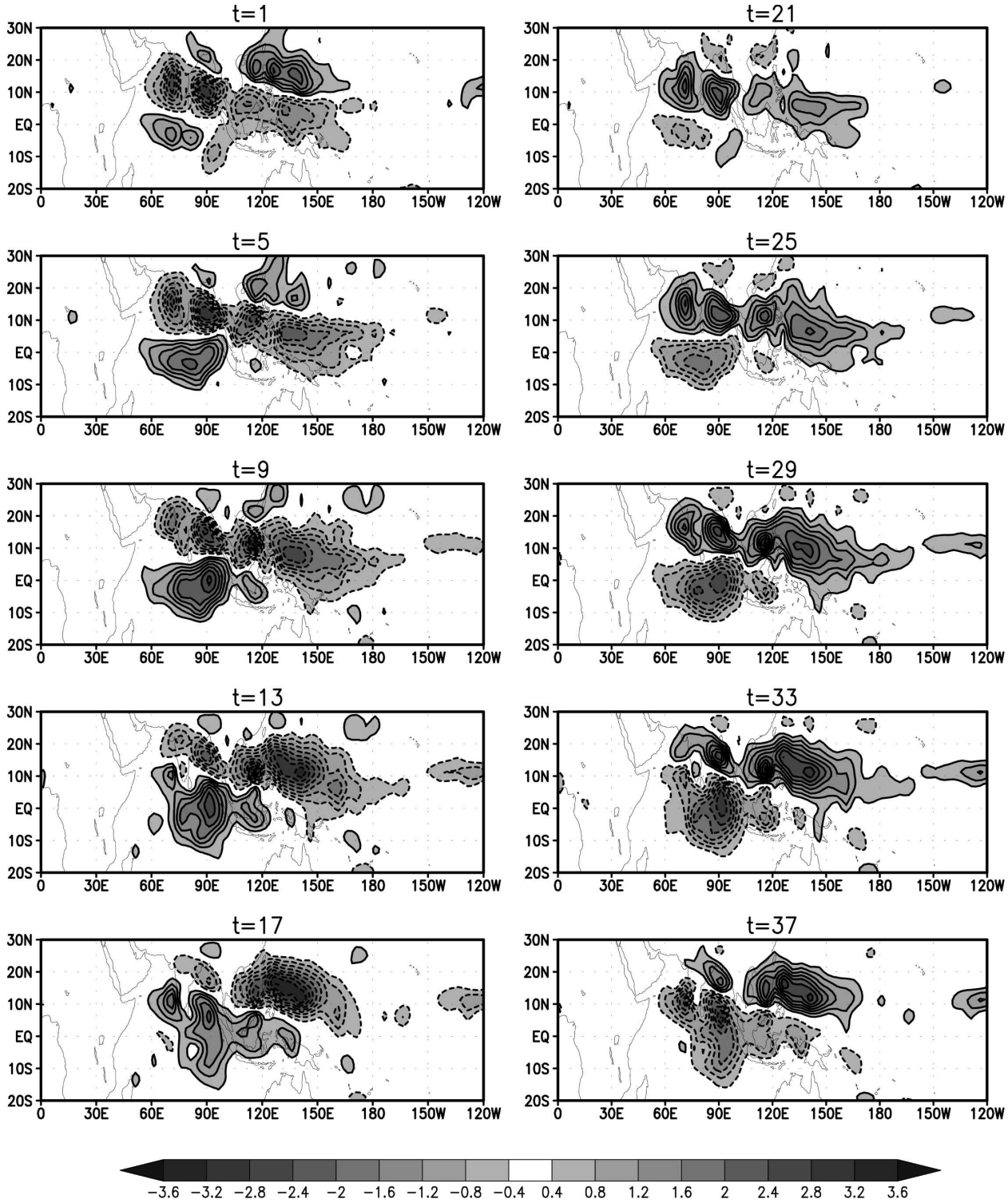

FIG. 5. Life cycle of the observed BSISO convection anomalies. This corresponds to the first EEOF mode of CMAP precipitation for the 1982–2002 JJAS. The contour interval is 0.4 mm day^{-1}.

(115°E), and finally the WNP (130°–140°E), which form the peaks of intraseasonal variance along 15°N as shown in Fig. 4 (Hsu et al. 2004). The slanted precipitation band with the four distinct deep convection centers can be seen at t = 25–29. A virtually identical life cycle is also obtained with an EOF analysis of the Advanced Very High Resolution Radiometer (AVHRR) OLR (see Fig. 14 of Seo et al. 2005).

To simulate the timing of the break and active phases of the Asian summer monsoon, it is desirable that a climate model be capable of simulating this variability realistically. The corresponding time evolution of the BSISO convection anomalies simulated in GFS and CFS can be seen in Fig. 6. For brevity, only the half cycle is presented. The figure shows that both runs do not simulate the overall evolution pattern as seen in the previous canonical life cycle of the BISIO convection. The characteristic northward propagation over the Indian Ocean is not well captured. The rainfall anomaly at the equator in the eastern Indian Ocean in GFS does not expand to the north. In CFS, the rainfall anomaly in the equatorial eastern Indian Ocean tends to slowly propagate to the north but it dies off at 7°–8°N. This weakening is due to the cold bias present in the model (Fig. 3). The convection anomaly separately formed at 10°N in the eastern Indian Ocean also tends to propagate slowly northward. But there is no continuous northward propagation as seen in the observation. Also, it is noticed that eastward propagation along the equator is not well simulated. The longitude–time plot will be presented later.

b. *Mechanism of northward propagation of the BSISO anomalies*

It has been suggested that the northward propagation of the BSISO convection is a result of the systematic interaction of convection, surface dynamics, thermodynamics, and radiation (e.g., Kemball-Cook and Wang 2001). Here we investigate phase relationships between the BSISO convection and other surface variables. For this, the analyzed variables are regressed against the principal component of the first EEOF mode of precipitation. Figure 7 shows the evolution of 65°–95°E average of observed surface zonal wind, latent heat flux, shortwave radiation flux, surface temperature, surface vorticity, and surface moisture convergence (all contoured) relative to CMAP precipitation (shaded). The moisture convergence is defined as $-\nabla \cdot (\mathbf{V}q)$, where $\mathbf{V}$ is the velocity vector and q is the specific humidity. The lead–lag time is assigned such that rainfall peak at the off-equator region (12°–15°N) occurs at zero lag.

The westerly anomalies exist under deep-precipitating BSISO convection while the easterly anomaly develops to the north of this convection (Fig. 7a). Over the entire region, JJAS mean low-level zonal winds are westerlies as shown in Fig. 2a, and therefore, to the north of the convection, the zonal wind anomaly tends to decrease total wind speed, leading to reduced evaporation from the ocean to the atmosphere. Consequently, anomalous latent heat flux is downward (downward flux is defined positive; Fig. 7b). Also, suppressed convection associated with the negative rainfall anomalies results in a positive downward solar radiation at the surface (Fig. 7c). Both latent heat and solar radiation fluxes act to heat the surface (Fig. 7d). The positive SST anomaly precedes convection anomaly by 1/4 cycle (~10–12 days). Also, the maximum positive surface vorticity (Fig. 7e) is located to the north of the enhanced convection center. In Fig. 7e, from day −15 through −10 a tropical vorticity dipole exists due to the equatorial convective heating. The positive vorticity around lag 0 represents the onset of the active phase the Indian monsoon because it deepens climatological trough over this region. The peak moisture convergence (solid line in Fig. 7f) appears to the north of the convection anomaly (dashed line). This relationship between moist convergence and convection is consistent with the findings from previous studies (e.g., Kemball-Cook et al. 2002), suggesting that this lag relationship is important for northward propagation. The BSISO convection moves northward toward the region of maximum moisture convergence and anomalous surface heating. Hence, the northward propagation of BSISO convection is associated with both convection–circulation interaction and atmosphere–ocean coupling. Interestingly, in the Southern Hemisphere, the surface moisture convergence also leads southward-propagating convection anomaly that eventually disappears after it moves to the region of cooler SSTs and westerly vertical shear region.

For the GFS simulation, the first two modes for precipitation explain only 6% of the total bandpass-filtered rainfall variability. Figure 8 shows that the northward propagation of rainfall is not well simulated in GFS: the BSISO convection anomaly does not show an initiation over the equatorial Indian Ocean and a strong standing oscillation of the convection dominates (Fig. 8). Because of the use of specified SST for the oceanic surface, there is no surface temperature variability to the south of 15°N (Fig. 8d), which is purely ocean surface. The relatively large surface temperature variability to the north of 15°N is mainly due to the variation of land skin temperatures (Fig. 8d), which is interactive in the

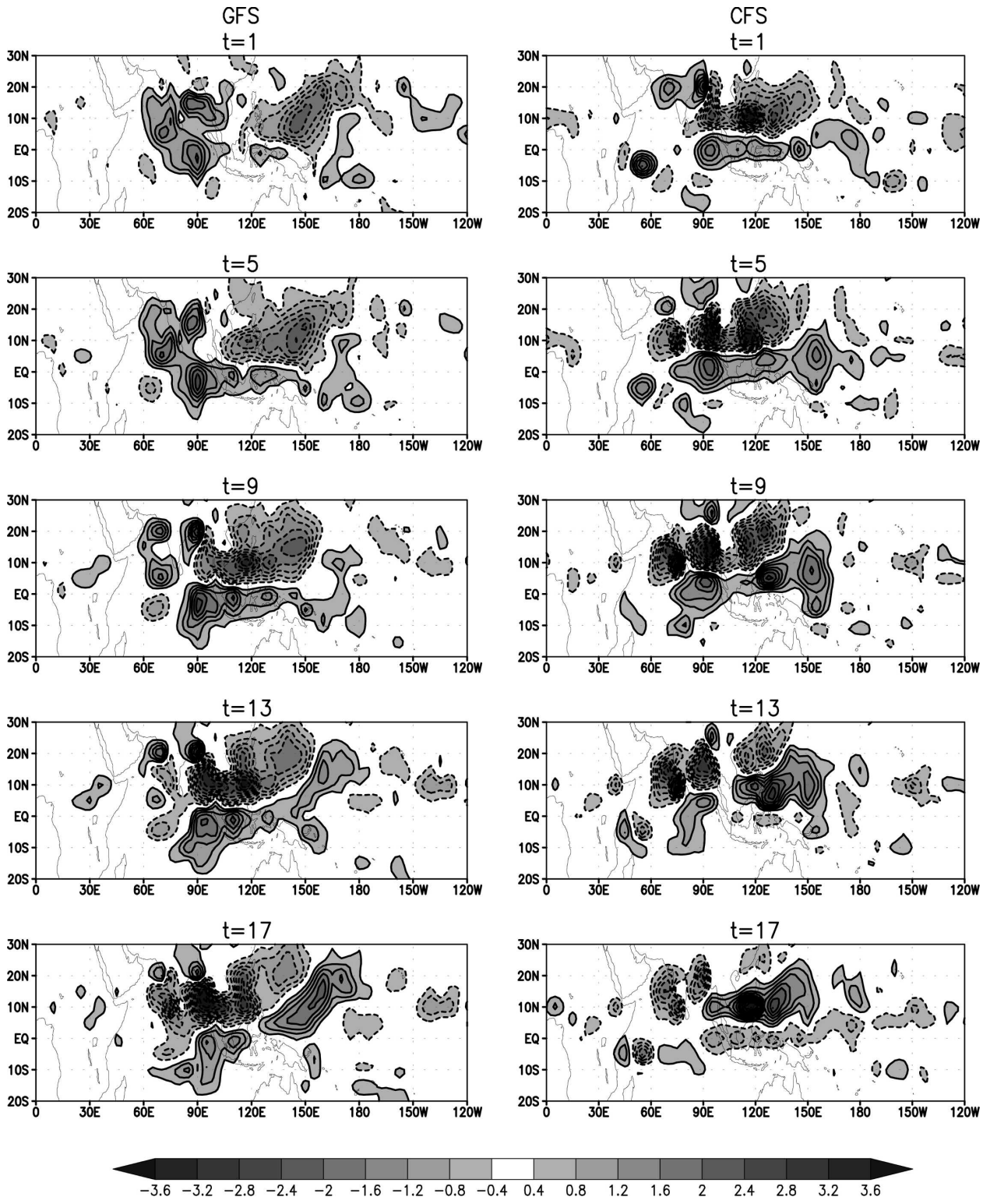

FIG. 6. Life cycle of BSISO convection anomalies in (left) the GFS and (right) the CFS. This corresponds to the half cycle of the first extended EOF mode of precipitation for 23-yr JJAS. The contour interval is 0.4 mm day^{-1}.

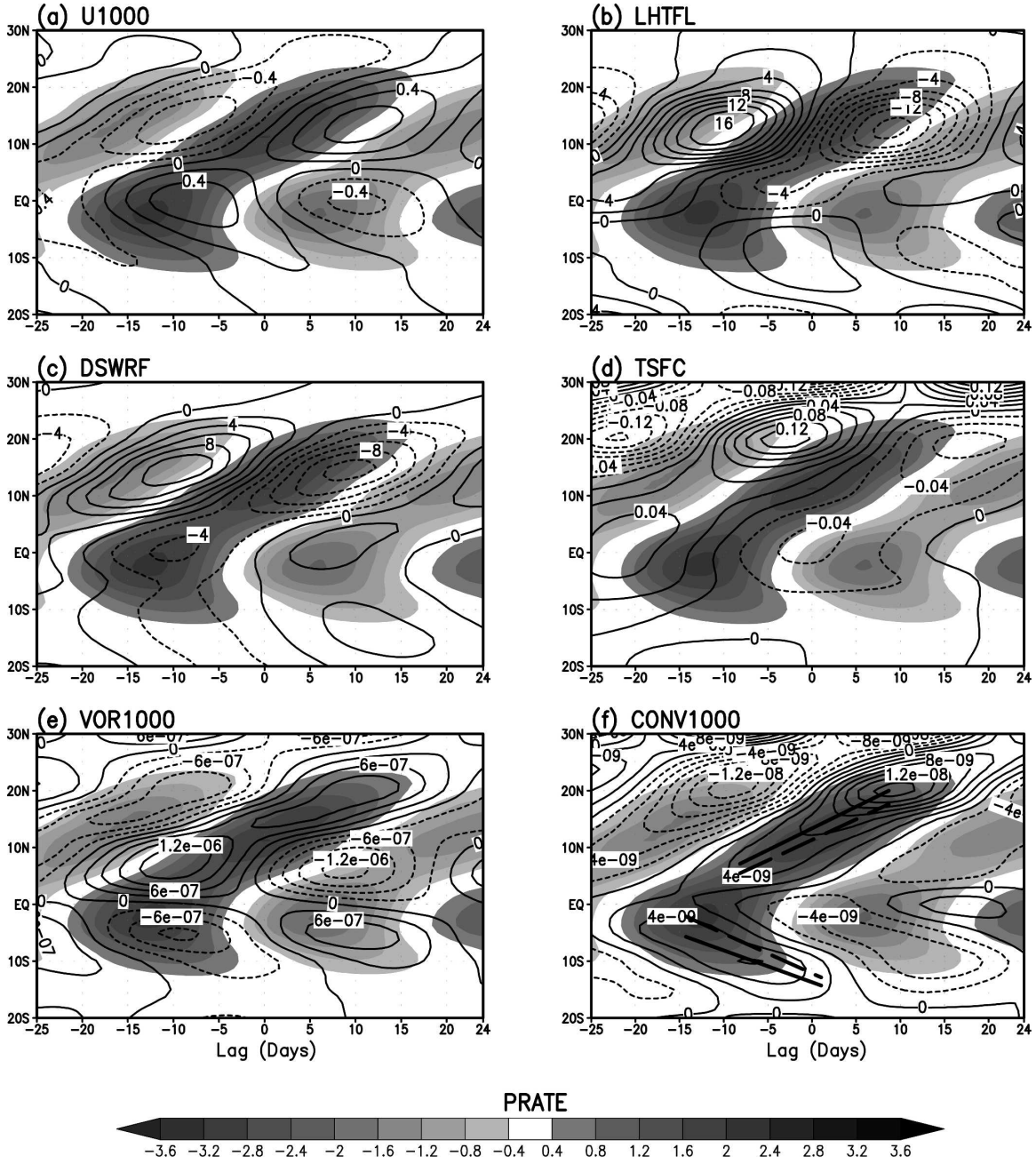

FIG. 7. Time–latitude plots of observed precipitation anomalies (shaded) with (a) 1000-hPa zonal wind, (b) surface latent heat flux, (c) downward solar radiation flux, (d) skin temperature, (e) 1000-hPa vorticity, and (f) 1000-hPa moisture convergence. The contour intervals are 0.2 m s^{-1} for 1000-hPa zonal wind, 2 W m^{-2} for surface heat fluxes, 0.02 K for the surface temperature, 3×10^{-7} s^{-1} for 1000-hPa vorticity, and 2×10^{-9} kg s^{-1} kg^{-1} for 1000-hPa moisture convergence. All variables are averaged over a longitudinal band of 65°–95°E. In (f), the thick solid line denotes the location of peak moisture convergence and the dashed line denotes the location of peak precipitation.

model. The surface heat and radiation fluxes (Figs. 8b,c) in this simulation do not determine the SST variation.

In the CFS simulation (Fig. 9), the first two precipitation modes account for 6.5% of total variability. As seen in Fig. 6, two separate northward-propagation anomalies are noticed but they still exhibit standing behavior. However, CFS shows the overall correct phase relationships among the variables. For example, on the northern side of the precipitation anomaly, the

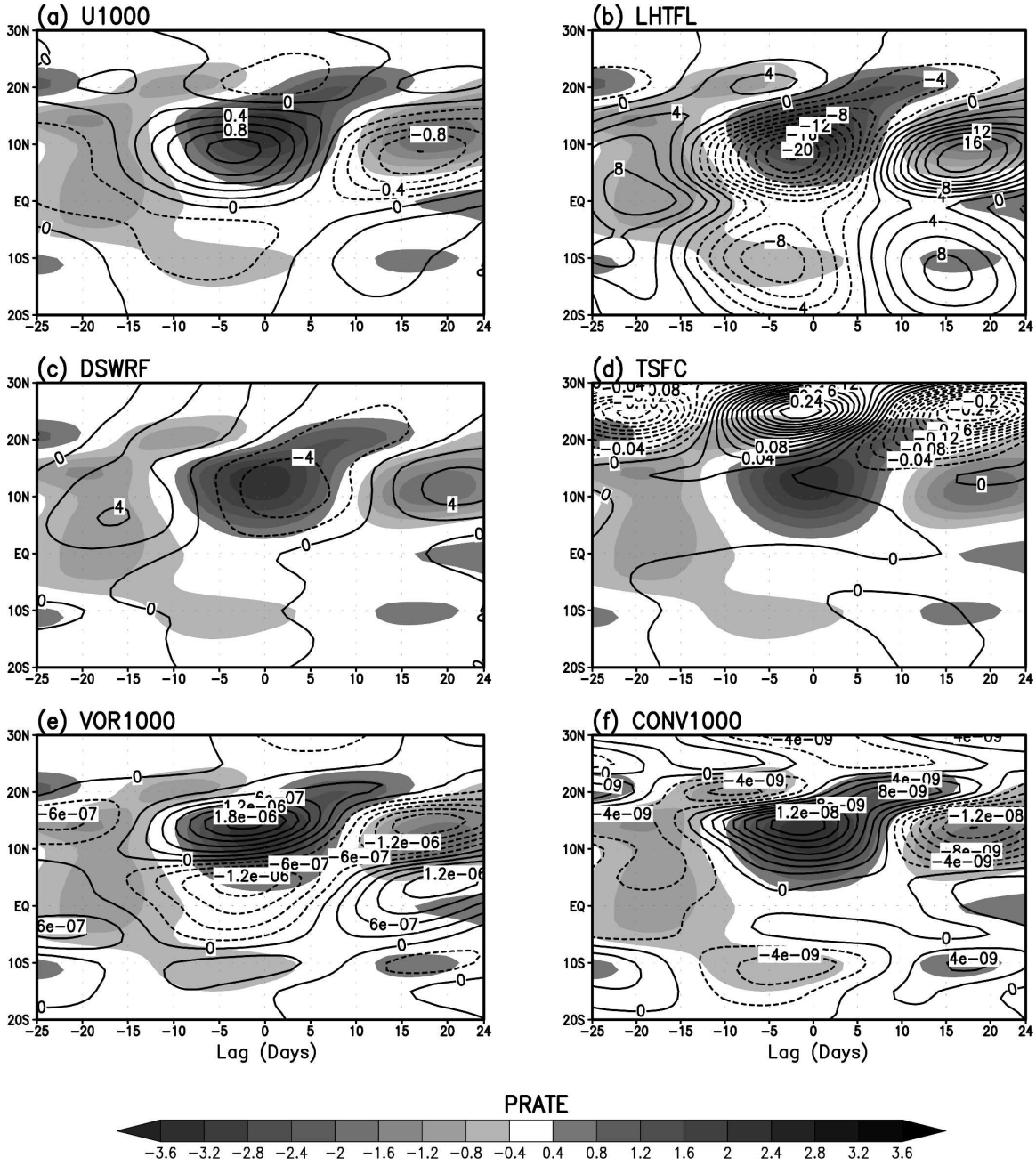

FIG. 8. Time–latitude plots of precipitation anomalies (shaded) with (a) 1000-hPa zonal wind, (b)the surface latent heat flux, (c) the downward solar radiation flux, (d) the skin temperature, (e) 1000-hPa vorticity, and (f) 1000-hPa moisture convergence in the GFS simulation. The contour intervals are 0.2 m s^{-1} for 1000-hPa zonal wind, 2 W m^{-2} for the surface heat fluxes, 0.02 K for the surface temperature, 3×10^{-7} s^{-1} for 1000-hPa vorticity, and 2×10^{-9} kg s^{-1} kg^{-1} for 1000-hPa moisture convergence. All variables are averaged over a longitudinal band of 65°–95°E.

easterly anomaly develops as in the observation. Since the model-simulated JJAS mean 1000-hPa zonal winds in CFS are also westerlies over the northern tropical regions (Fig. 2b) as in the observation (Fig. 2a), this easterly anomaly tends to enhance downward latent heat flux (or reduced evaporation). Also, the surface solar radiation is positive due to the negative cloud amount. Both flux components lead to an increase in surface temperature. Peak positive surface vorticity and moisture convergence are also located slightly to the

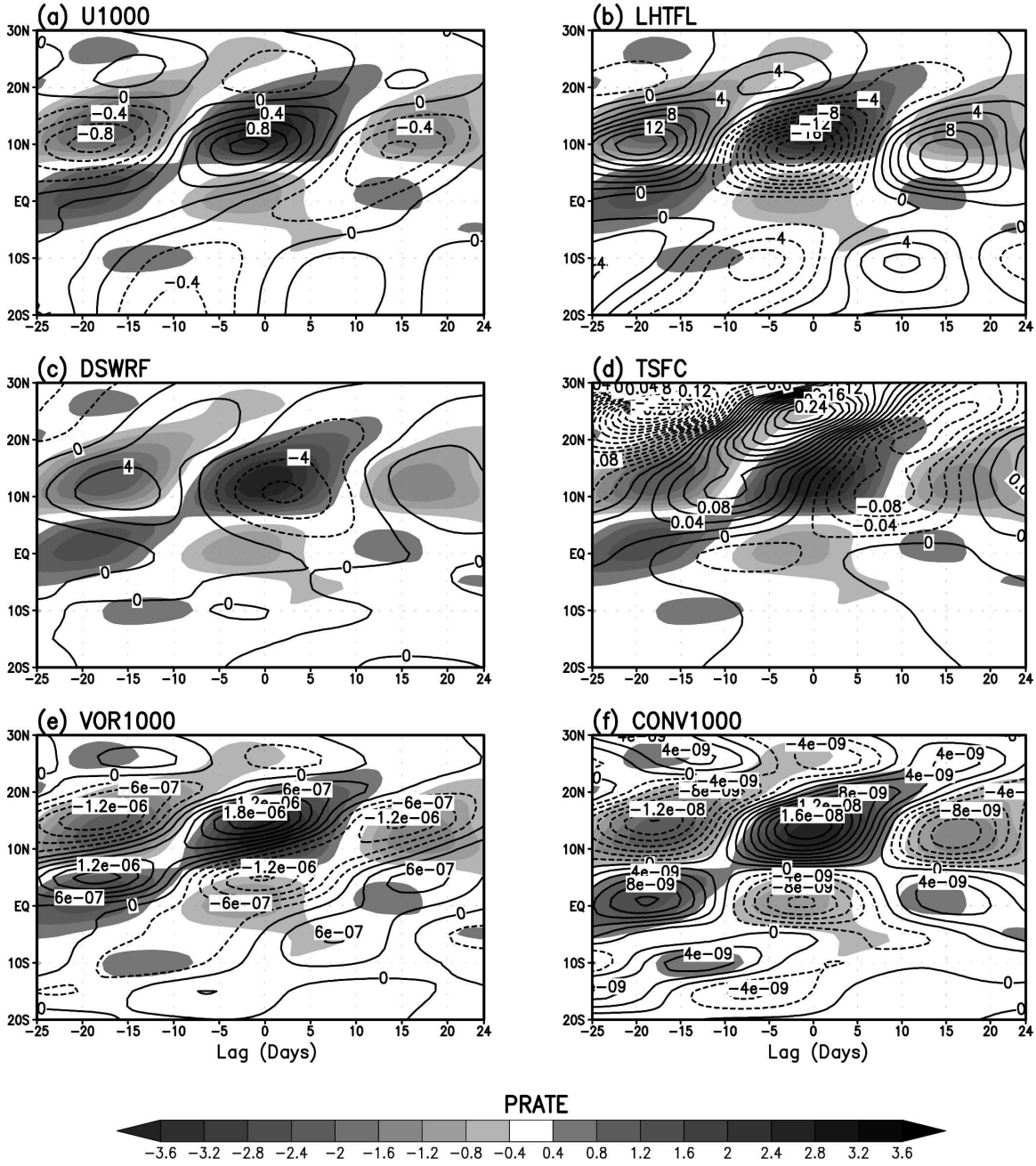

FIG. 9. Same as in Fig. 8, but for the CFS simulation.

north of the convection anomaly as in the observations. Therefore, the inclusion of air–sea interaction in CFS shows some limited improvements.

c. Eastward-propagating equatorial mode

The BSISO also contains an eastward-propagating equatorial mode. As seen in Fig. 5, tropical diabatic heating forces a Kelvin–Rossby wave packet and most of the northward propagation coexist with the eastward propagation of the Kelvin wave along the equator (Lawrence and Webster 2002; Hsu et al. 2004). To further confirm this, the time evolution of precipitation, surface temperature and surface moisture convergence averaged over 5°S–5°N is plotted for the observation and the model simulations in Fig. 10. It is evident that the observed precipitation anomaly propagates eastward from the Indian Ocean across the west Pacific.

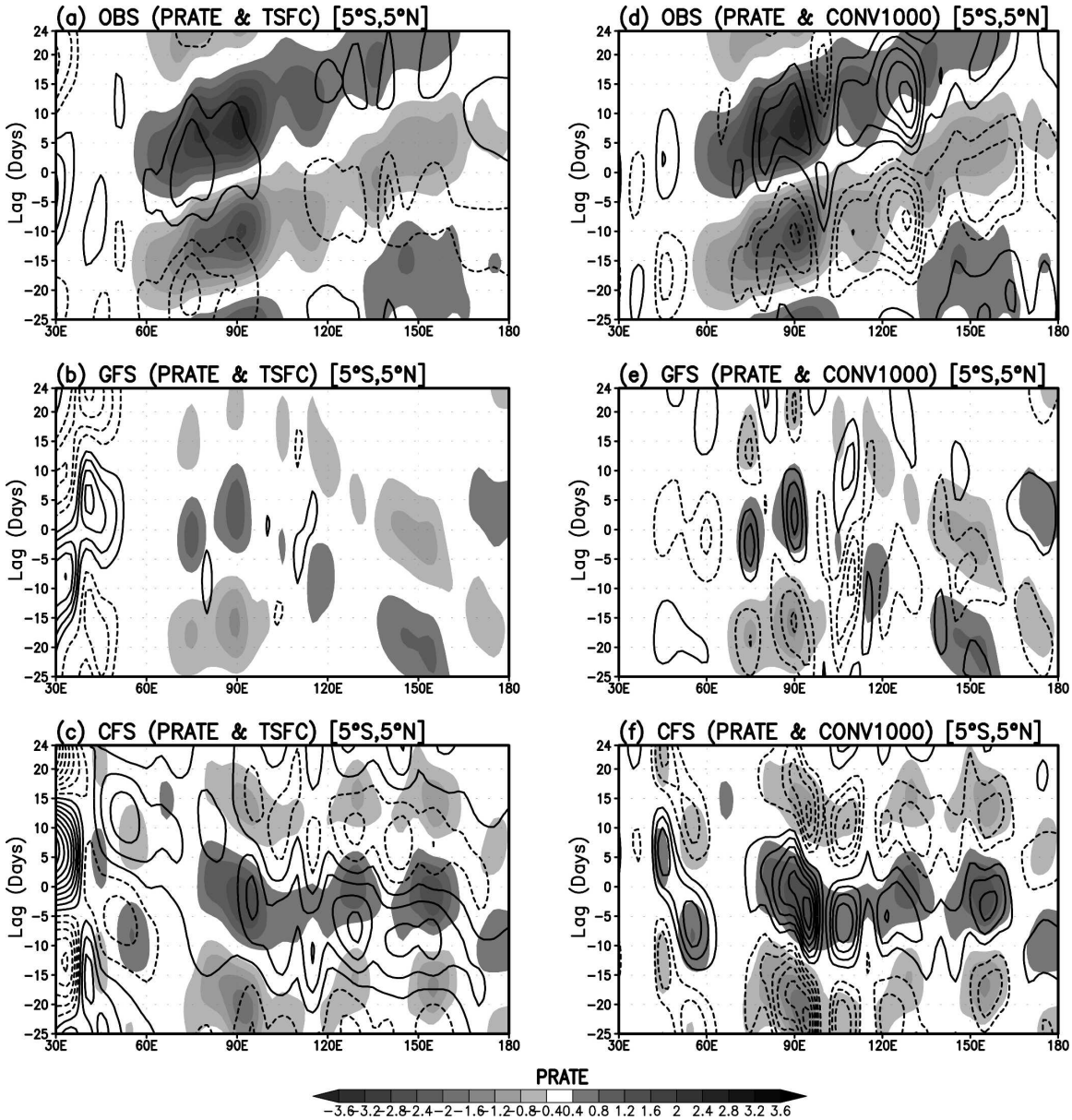

FIG. 10. Longitude–time plots of precipitation anomalies (shaded) along with surface temperature (contours) in (a) the observation, (b) GFS, and (c) CFS, and with 1000-hPa moisture convergence (contours) in (d) the observation, (e) GFS, and (f) CFS. The contour interval for the surface temperature is 0.02 K and is 2×10^{-9} kg s^{-1} kg^{-1} for the moisture convergence. The zero lines are depressed. All variables are averaged over an equatorial strip of 5°S–5°N.

The propagation is a bit faster over the west Pacific probably due to decreased diabatic heating in that region. The observed intraseasonal surface temperature anomaly propagates eastward (Fig. 10a) and leads the precipitation anomaly by a quarter cycle (~10–12 days). Surface moisture convergence, although noisier, also propagates eastward. Over the Indian Ocean, surface moisture convergence is nearly in phase with the precipitation anomaly but over the Maritime Continent and western Pacific, the enhanced convection anomaly is preceded by the surface moist convergence, in accordance with the frictional wave-conditional instability of the second kind (CISK) mechanism along the equator (e.g., Wang and Rui 1990; Waliser et al. 1999; Seo and Kim 2003). In both GFS and CFS, however, the eastward-propagating signal for the surface temperature, moist convergence, and convection anomalies are not prominent over the Indian Ocean, and both tend to simulate the westward-propagating anomalies across the west Pacific. The possible reason for this erroneous

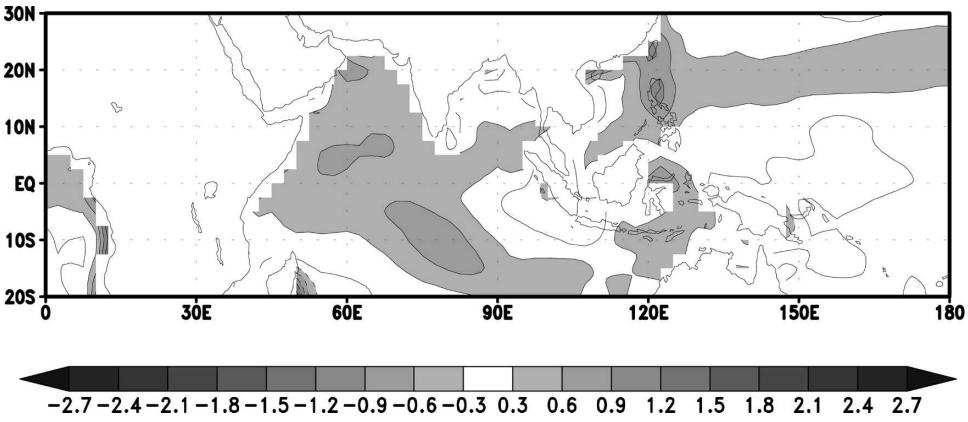

FIG. 11. JJAS mean SST difference (K) between the CFSA run and the observation. The contour interval is 0.3 K.

feature is studied in the next section using a flux-corrected CFS simulation.

5. Flux-corrected CFS simulation (CFSA)

The cold bias over the eastern Indian Ocean in CFS tends to weaken the convection anomaly. Consequently, in the CFS simulations the coherent northward-propagating convective mode and eastward-propagating convective mode along the equator do not exist. To investigate if this is due to SST bias in the coupled simulations, a flux-corrected coupled simulation is analyzed. As will be shown, the reduction in SST bias with the flux correction results in more realistic northward propagation over the Indian Ocean. This also improves the basic-state dynamical conditions, giving rise to more realistic eastward propagation of the BSISO along the equator over the Indian Ocean.

Figure 11 shows the SST bias from the CFS simulation with flux adjustments. The main warm bias seen over the western Indian Ocean in the CFS simulation (Fig. 3) disappears. More importantly, a cold bias in the equatorial eastern Indian Ocean and Java Sea is also eliminated, leading the reduced easterly surface zonal wind bias by a factor of ~2 (Fig. 12). Another region with cold bias along the ITCZ in the WNP (10°–20°N, 120°–150°E) is also improved. This correction in turn results in the recovery of the seasonal mean convection in the WNP (Fig. 13). In addition, the peak location of the mean convection in the southern Indian Ocean is improved (similarly the improvement in the peak region of intraseasonal variability over this region is also evident, not shown)

Along with the reduced surface zonal wind bias, the strong easterly shear in the equatorial Indian Ocean and western Pacific, which was not well simulated in CFS, becomes more realistic in CFSA as shown in Fig. 13 (although it is still in smaller magnitude than the observation). Both enhanced westerlies at the lower level and increased easterlies at the upper level (not shown) contribute to this strengthening. Note that the wind shear in GFS (Fig. 1b) is similar to CFSA. This

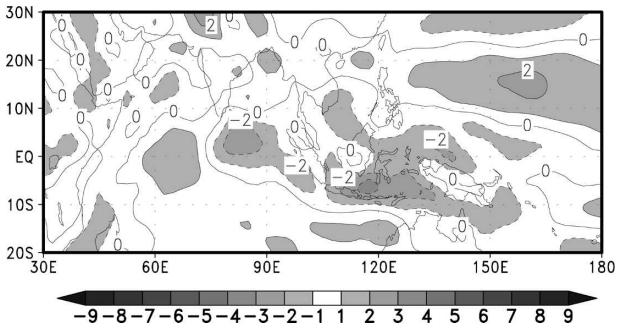

FIG. 12. JJAS mean 1000-hPa zonal winds (m s^{-1}) for the difference between the CFSA run and the observation. The contour interval is 1 m s^{-1}.

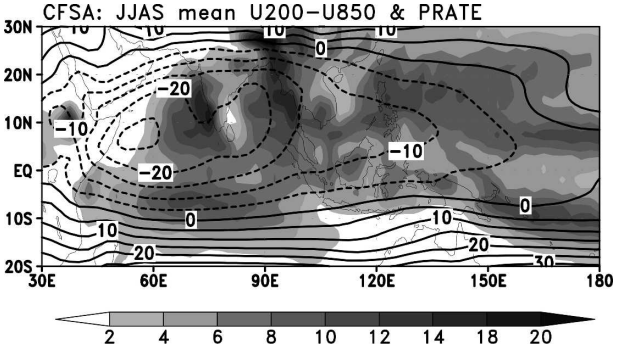

FIG. 13. JJAS mean precipitation rate (mm day^{-1}, shaded) and vertical shear of zonal winds (U200–U850, contours) from the CFSA run. The contour interval is 5 m s^{-1}.

indicates that the errors in the vertical wind shear in the Indian Ocean and western Pacific in the CFS simulation are related to the errors in the simulated seasonal mean SST.

Figure 14 shows the time evolution of BSISO rainfall anomalies in CFSA. The onset, development, and propagation of the convection anomalies are very similar to the observation (Fig. 5). First, the enhanced convection is initiated at the central Indian Ocean as in the observation and it develops further owing to the corrected mean-state SST. The enhanced and suppressed convection anomalies exhibit the observed quadrupole-like pattern during $t = 1$ to $t = 9$ (see Fig. 5). The northward propagation of the convection anomaly over the Indian sector is evident. The steady, continuous northward propagation can also be seen in the time–latitude plot averaged over the Indian Ocean (65°–95°E; Fig. 15). It is seen in Fig. 14 that while northward propagation in the Indian Ocean is improved in CFSA, the simulation of northward propagation in the west Pacific remains poor when compared to the observation (Fig. 5). This is associated with significantly decreased activity of the eastward-propagating equatorial convection anomaly in the west Pacific (see also Fig. 17) since the convection anomaly propagated from the Indian Ocean into the west equatorial Pacific can exhibit subsequent northward propagation as in the observation (see Fig. 5).

Figure 15 shows the northward-propagating convection mode and its relationships with surface zonal winds, heat fluxes, temperature, vorticity, and moist convergence. It is obvious that the gross features of phase relationships are in close agreement with the observations (Fig. 7). The downward surface latent heat and solar radiation fluxes lead to the positive surface temperature anomaly north of the convection anomaly. The maximum surface vorticity and moisture convergence are located to the north of the enhanced convection as in the observations. This surface moisture convergence is maybe regarded as one of the most important factors for the maintenance and propagation of the BSISO, similarly to the winter MJO case (Waliser et al. 1999). To further investigate which component of moisture convergence is more important, the zonal and meridional components of moisture convergence are separately calculated and are shown in Fig. 16. For observations as well as in the CFSA (also in CFS, not shown), the meridional convergence appears consistently to the north of the propagating convection anomaly. In fact, this meridional convergence is due to the southwesterly flow and acts to intensify the climatological "cross-equatorial" southwesterly monsoon flow, leading to the

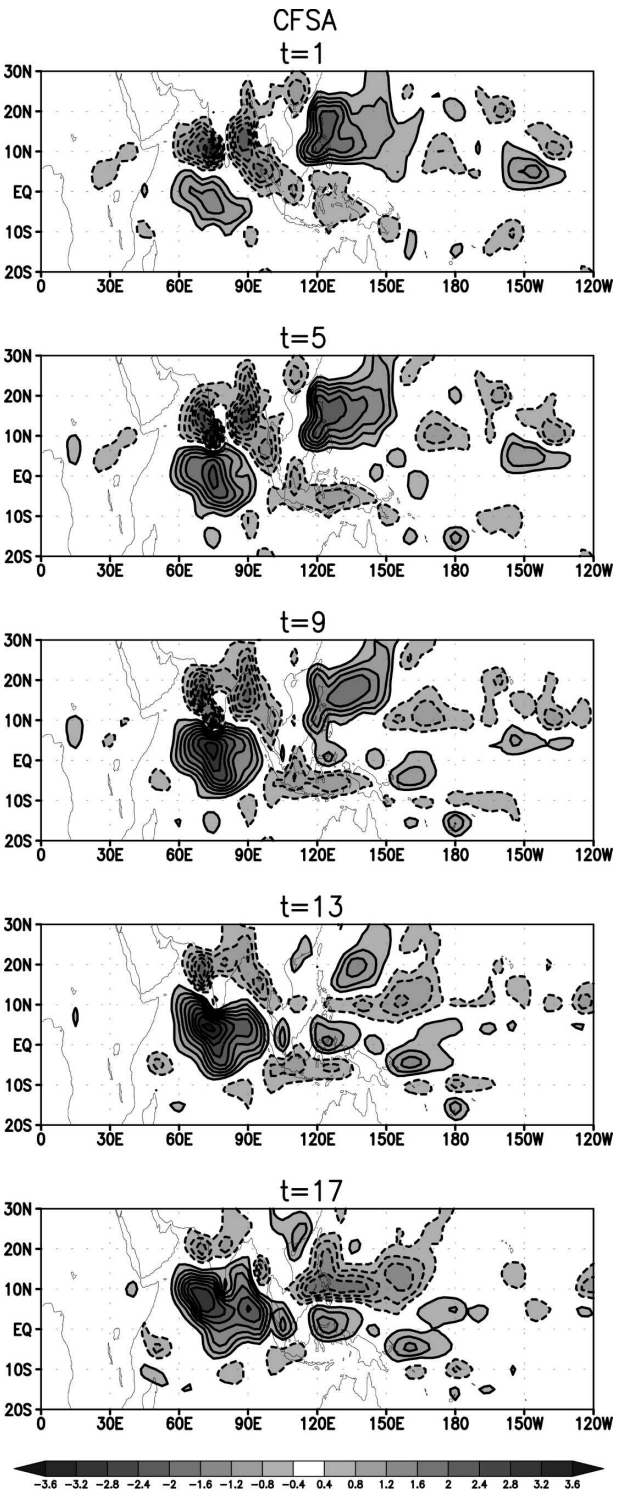

FIG. 14. Life cycle of the BSISO convection anomalies in CFSA. This corresponds to the half cycle of the first extended EOF mode of precipitation for the 21-yr JJAS. The contour interval is 0.4 mm day^{-1}.

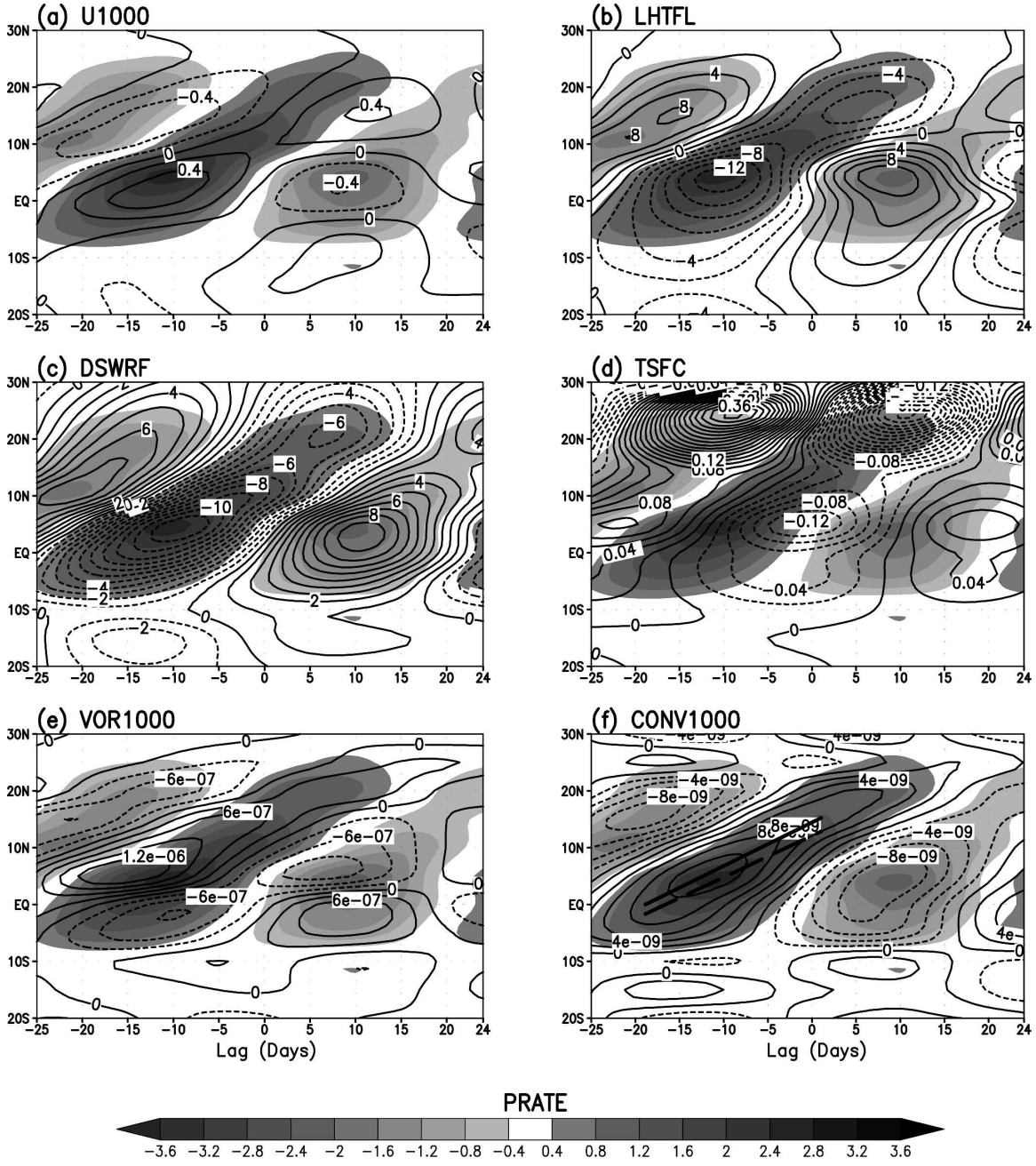

FIG. 15. Same as in Fig. 7, but for the CFSA simulation.

active phase of south Asian monsoon. Therefore, as in the winter MJO, the BSISO propagation is a result of the interaction between circulation and convection. The proper simulation of the meridional moist flux requires the proper simulation of the basic-state features and air–sea interaction.

Again, the results demonstrate that the improved large-scale mean state in SST, low-level winds, and vertical wind shear under interactive air–sea coupling leads to an improved simulation of the northward propagation, spatial patterns, and time evolution of BSISO anomalies. The improved mean state also produces better simulation of eastward-propagating equatorial mode. Figure 17 shows the 5°S–5°N averaged rainfall anomaly along with surface temperature and surface moist convergence. It is seen that a positive intraseasonal SST anomaly leads the convection anomaly by a quarter cycle over the Indian Ocean (Fig. 17a) as in the

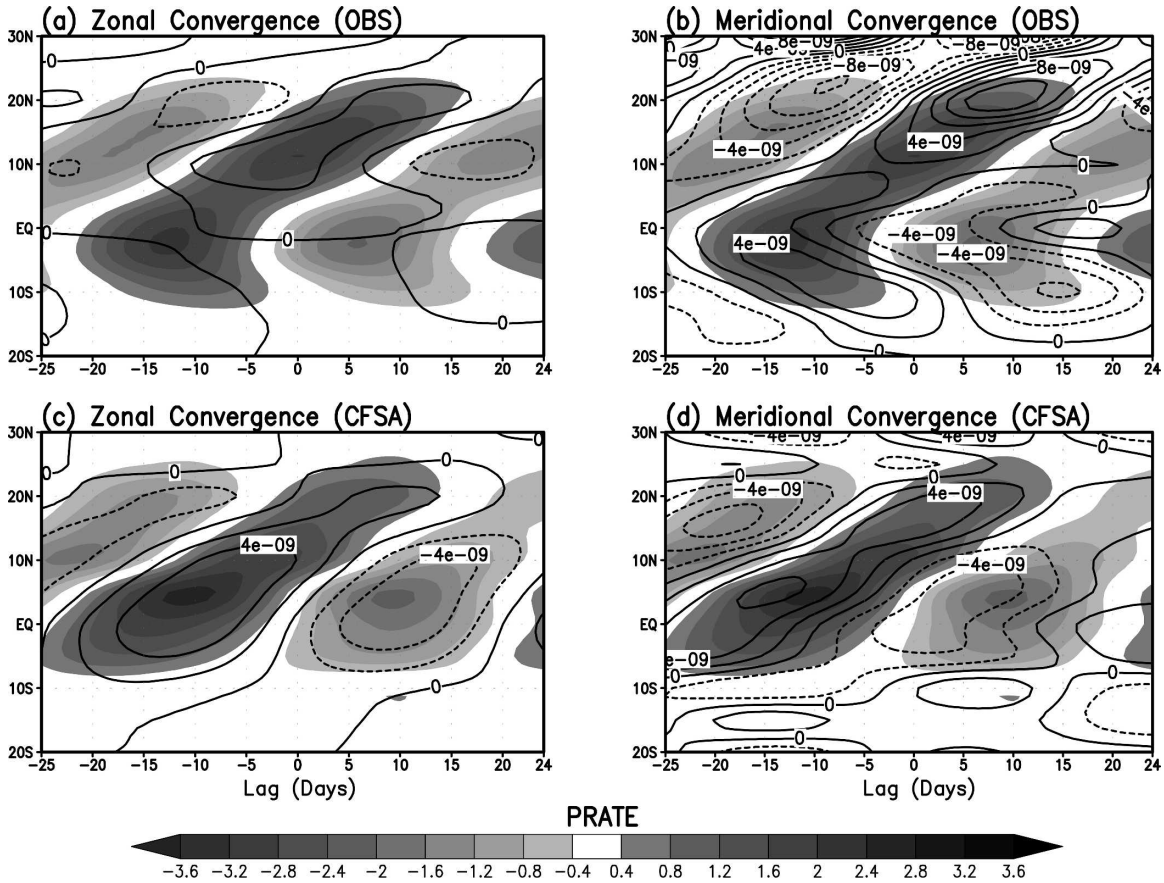

FIG. 16. Time–latitude plots of precipitation anomalies (shaded) with (a) zonal and (b) meridional moisture convergence at 1000 hPa in the observation, and (c) zonal and (d) meridional moisture convergence at 1000 hPa in the CFSA. The contour intervals are 2×10^{-9} kg s^{-1} kg^{-1}. All variables are averaged over a longitudinal band of 65°–95°E.

observation (Fig. 11a). Also the surface moist convergence is collocated with the enhanced convection anomaly over the Indian Ocean, similar to the observations.

One clear deficiency in the CFSA simulation is that the eastward-propagating mode abruptly halts across the western Pacific near 140°E. A similar difficulty was remedied in a flux-corrected coupled run for boreal winter seasons by Inness et al. (2003). They suggested that the errors in the low-level zonal wind were responsible for the failure of the equatorial MJO propagation into this region rather than the errors in SST. In our case (CFSA), as the SST errors in this region are small, this may not be the cause for this deficiency. The possible causes for this are discussed in the following section.

6. Summary and discussion

The effects of air–sea coupling and basic-state SST associated with the boreal summer intraseasonal oscillation are investigated by comparing the long-term simulations with the NCEP uncoupled model (GFS), fully coupled model (CFS), and the CFS run with flux corrections (CFSA). The GFS simulation shows disorganized BSISO convection anomalies, and these exhibit an erroneous standing oscillation. The CFS simulation shows some limited improvements compared to the GFS, but the inclusion of coupled air–sea coupling does not result in the observed continuous northward propagation over the Indian Ocean. This was shown to be due to a cold SST bias. Improvements in the CFS simulation include the correct phase relationships between precipitation and the intraseasonal SST oscillation, and the enhanced northward propagation over the western Pacific. The flux-corrected CFSA run further removes a cold bias in the Indian Ocean, and thus, the development and propagation of the convection anomalies are significantly similar to the observation. The convection is initiated at the central Indian Ocean, as in the observation, and enhanced and suppressed convection anomalies exhibit the observed quadrupole-like con-

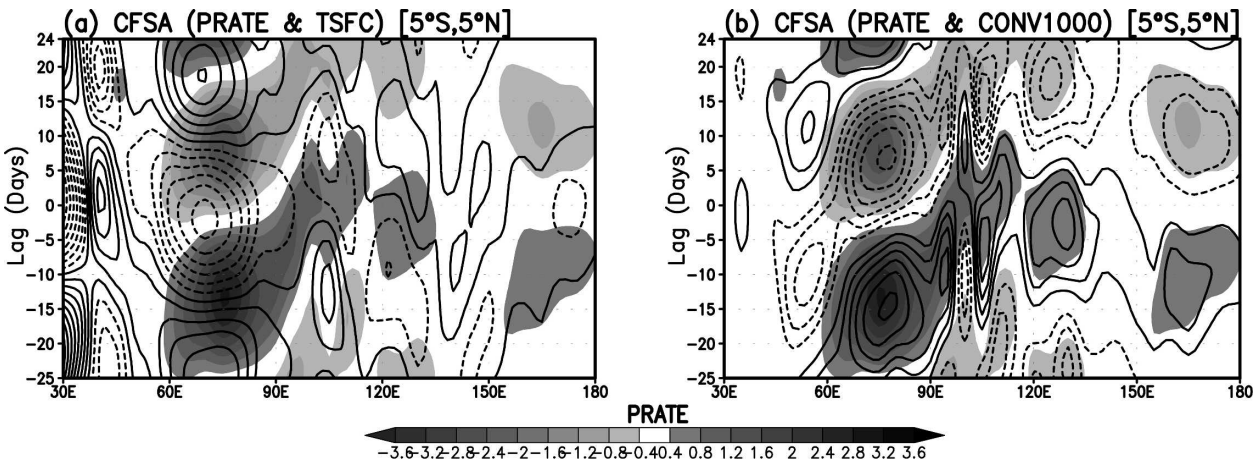

FIG. 17. Longitude–time plots of precipitation anomalies (shaded) along with (a) the surface temperature (contours), and (b) 1000-hPa moisture convergence (contours) in the CFSA run. The contour interval for the surface temperature is 0.02 K and is 2×10^{-9} kg s^{-1} kg^{-1} for the moisture convergence. The zero lines are depressed. All variables are averaged over an equatorial strip of 5°S–5°N.

figuration. The steady, continuous northward propagation of the convection anomaly over the Indian Ocean is also well simulated. This also results in the coherent, correct phase relationships between precipitation and surface dynamic and thermodynamic variables for the northward propagation: 1) the near-surface easterly wind to the north of the equatorial convection decreases total wind speed and reduces evaporation from the ocean to the atmosphere, resulting in anomalous downward latent heat flux; 2) in relation to suppressed convection at ~10°N, a positive downward shortwave radiation flux anomaly develops and this radiation flux is as strong as the induced latent heat flux as in the observation; 3) these surface fluxes induce a positive surface heating leading the convection by a quarter cycle (~10 days); and 4) the peak horizontal surface moisture convergence consistently develops along the north of the northward-propagating enhanced convection center. Thus, the analysis implies that coupled air–sea interaction plays a key role in the development and maintenance of the BSISO as long as mean SST biases are small. It is also shown that the surface meridional moisture transport convergence is the most important contributing factor in moisture flux convergence and hence in the propagation of the BSISO. Thus, it is concluded that the northward propagation of the BSISO is a result of convection–circulation coupling and atmosphere–ocean coupled interactions.

In contrast to the simulation of the northward propagation of the BSISO, both GFS and CFS do not realistically simulate the eastward-propagating equatorial mode. The CFSA run produces a more realistic eastward propagation mode only over the eastern Indian Ocean and Java Sea owing to the improved mean states in SST and vertical wind shear, suggesting the importance of mean SST and circulation fields. However, the propagation of this equatorial mode into the west Pacific remains unrealistic even in CFSA. Possible reasons include the following factors. First, the vertical shear of basic zonal wind in the western Pacific is smaller than the observation (Figs. 1a and 13). Second, the simulated equatorial low-level zonal wind in this region is relatively stronger easterly (Fig. 12) compared to the observed weak easterlies or westerlies (Fig. 2a). Third, the model resolution is rather coarse to resolve the Maritime Continent region. While these deficiencies are likely due to the imperfect model physics (e.g., cumulus parameterization and boundary layer treatment) sensitivity experiments are needed to find out the specific physics that are directly related to the simulation errors. Last, the errors in the simulated eastward propagation may also be related to the nature of the seasonality of the observed intraseasonal variability. The observation shows a weaker eastward-propagating precipitation signal in boreal summer than the boreal winter counterpart (e.g., Wheeler and Hendon 2004; Zhang and Dong 2004). Consequently, it is more difficult to simulate the eastward component during northern summer than in northern winter. In fact, the simulation of the propagation of the MJO from the Indian Ocean across the western Pacific in the northern winter is improved in the CFS with flux correction (not shown; this will be reported elsewhere), as in the Third Hadley Centre Coupled Ocean–Atmosphere General Circulation Model (HadCM3) by Inness et al. (2003). The errors in SST are not considered to be a reason for the failure of the simulation of the northern summer eastward propagation in the western Pacific since the SST

errors are quite small as shown in Fig. 11 and the mean state in CFSA is very similar to that in GFS (Figs. 1b, 2b, 12, and 13). This study is unable to address which factor among those mentioned above is most important. Of course, this subject is beyond our scope and additional experimental simulations and thorough analysis are needed.

This study supports the hypothesis that air–sea coupling plays a role in the BSISO dynamics (e.g., Kemball-Cook et al. 2002; Fu et al. 2003) because the correct intraseasonal SST variation can only occur with interactive air–sea coupling. This is so because only in the case of coupled interactions does the sea surface feel the existence of the atmospheric ISO convective entity and respond consistently to the surface heat flux anomalies. The results suggest that the appropriate representation of seasonal mean SST is also necessary for the development and maintenance of the BSISO. This is because correct mean SSTs are required to sustain convection itself and to maintain realistic large-scale dynamical environment (i.e., easterly wind shear or low-level westerly zonal wind) favorable for the propagation of a coupled Rossby–Kelvin wave packet (Wang and Xie 1997).

Another way to examine the impact of air–sea interaction is to compare the real-time forecasts between GFS and CFS. Since there appear to be some improved aspects in the coupled model simulation, one would expect an improvement in the forecast of the northward propagation of the BSISO in the CFS compared to in the GFS. At NCEP, the CFS operational forecasts have been performed on a daily basis since fall of 2004. Here only a specific example is presented. A more comprehensive diagnostic will be reported on later.

Figure 18 shows 30-day forecasts of OLR (shading) and 850-hPa zonal wind anomalies (contour) from GFS and CFS initialized on 13 July 2005. Since the GFS model used is the same version as the atmospheric component of the CFS model, the differences in the forecast are due to the treatment of the ocean surface. To remove systematic model bias in the GFS and CFS forecasts, additional hindcast integrations were made for the recent 6-yr period from 1999 to 2004, and the anomalies are computed by removing the model climatology at the corresponding initial and the forecast lead time. The intraseasonal (30–70 days) signal is extracted by the method described in Seo et al. (2005). The observed analyses of the AVHRR OLR and R2 850-hPa zonal wind are also shown in Fig. 18a. For the observations, the enhanced convection propagates northward in the Northern Hemisphere, and the phase relationship between the convection and low-level wind anomalies is consistent with the previous discussion (see Fig. 7a). From the forecasts, it is apparent that the coupled CFS model produces the better evolution of these fields than the GFS model, indicating an enhance-

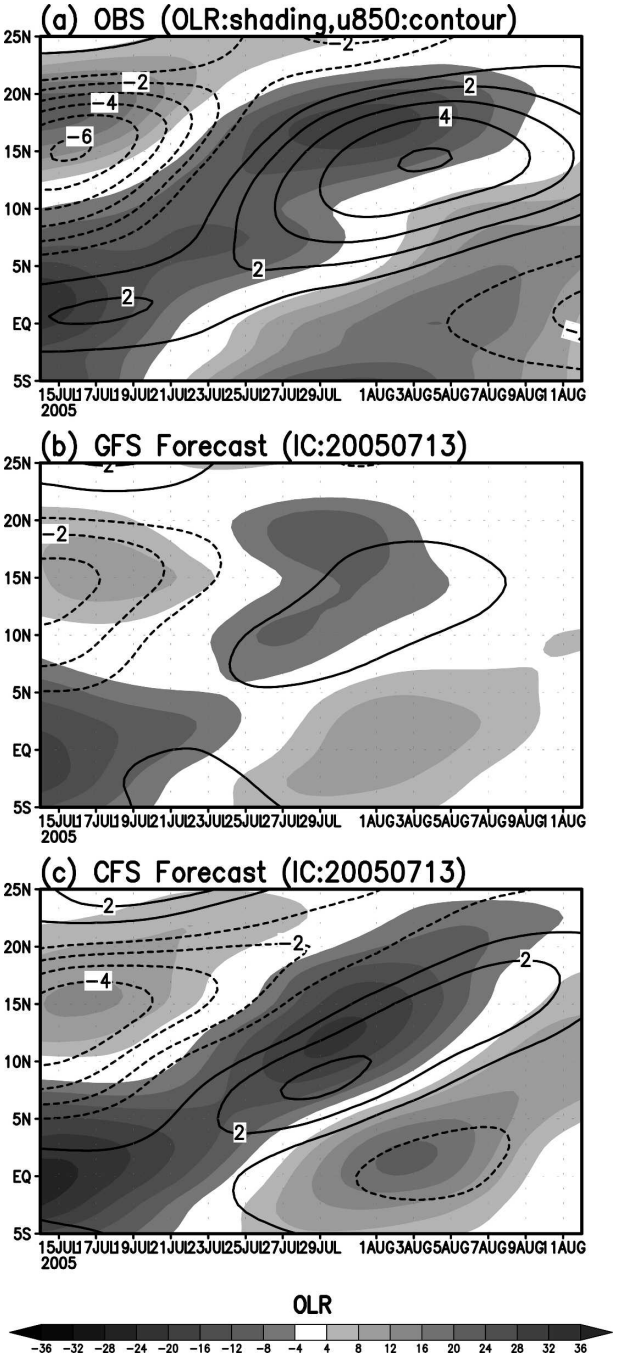

FIG. 18. Time–latitude plots of OLR (shading) and 850-hPa zonal wind (contour) anomalies for (a) the observations, (b) the GFS forecast, and (c) the CFS forecast. The forecast is initialized on 13 Jul 2005. The contour interval for the zonal wind is 1 m s^{-1} and the shading interval of OLR is 4 W m^{-2}. All variables are averaged over a longitudinal band of 65°–95°E.

ment of forecast performance because of the inclusion of the coupled air–sea interaction. More detailed evaluation of the prediction skill of the BSISO will be reported in the near future.

There are some limitations in this work. First, the results demonstrate that the improved large-scale basic-state dynamical fields in the low-level winds and vertical wind shear are important for the improved variability. However, without doing sensitivity tests, we cannot ascertain which components of the large-scale dynamical variables are most important. Second, Shinoda (2005) has showed that neglect of the diurnal cycle of surface fluxes could lead to an underestimation of warm SSTs during the dry, sunny phase of the ISO in the west Pacific. However, the coupling frequency is once a day in the current CFS integration and this configuration does not allow the examination of the impacts of diurnal cycle on SST. The dependency on the coupling frequency will be investigated when the configuration of the model becomes more flexible.

Acknowledgments. The authors thank Drs. P. Peng, Q. Zhang, and C. Long for their valuable comments and suggestions. We acknowledge the reviewers for their thorough reviews and insightful comments, which contributed greatly toward improving this paper.

REFERENCES

Annamalai, H., and J. M. Slingo, 2001: Active/break cycles: Diagnosis of the intraseasonal variability of the Asian Summer Monsoon. *Climate Dyn.,* **18,** 85–102.

Behringer, D., and Y. Xue, 2004: Evaluation of the global ocean data assimilation system at NCEP: The Pacific Ocean. Preprints, *Eighth Symp. on Integrated Observing and Assimilation Systems for Atmosphere, Ocean, and Land Surface,* Seattle, WA, Amer. Meteor. Soc., CD-ROM, P2.3.

Duchon, C. E., 1979: Lanczos filtering in one and two dimensions. *J. Appl. Meteor.,* **18,** 1016–1022.

Ferranti, L., T. N. Palmer, F. Molteni, and E. Klinker, 1990: Tropical–extratropical interaction associated with the 30–60 day oscillation and its impact on medium and extended range prediction. *J. Atmos. Sci.,* **47,** 2177–2199.

Flatau, M., P. J. Flatau, P. Phoebus, and P. P. Niiler, 1997: The feedback between equatorial convection and the local radiative and evaporative process: The implication for intraseasonal oscillations. *J. Atmos. Sci.,* **54,** 2373–2386.

Fu, X., and B. Wang, 2004: The boreal summer intraseasonal oscillation simulated in a hydrid coupled atmosphere–ocean model. *Mon. Wea. Rev.,* **132,** 2628–2649.

——, ——, T. Li, and J. P. McCreary, 2003: Coupling between northward-propagating, intraseasonal oscillations and sea surface temperature in the Indian Ocean. *J. Atmos. Sci.,* **60,** 1733–1753.

Hendon, H. H., 2000: Impact of air–sea coupling on the Madden–Julian oscillation in a general circulation model. *J. Atmos. Sci.,* **57,** 3939–3952.

——, and M. L. Salby, 1994: The life cycle of the Madden–Julian oscillation. *J. Atmos. Sci.,* **51,** 2225–2237.

——, and ——, 1996: Planetary-scale circulations forced by intraseasonal variations of observed convection. *J. Atmos. Sci.,* **53,** 1751–1758.

Hong, S.-Y., and H.-L. Pan, 1998: Convective trigger function for a mass-flux cumulus parameterization scheme. *Mon. Wea. Rev.,* **126,** 2599–2620.

Hsu, H.-H., and C.-H. Weng, 2001: Northwestward propagation of the intraseasonal oscillation in the western North Pacific during the boreal summer: Structure and mechanism. *J. Climate,* **14,** 3834–3850.

——, ——, and C.-H. Wu, 2004: Contrasting characteristics between the northward and eastward propagation of the intraseasonal oscillation during the boreal summer. *J. Climate,* **17,** 727–743.

Inness, P. M., and J. M. Slingo, 2003: Simulation of the Madden–Julian oscillation in a coupled general circulation model. Part I: Comparisons with observations and an atmosphere-only GCM. *J. Climate,* **16,** 345–364.

——, ——, E. Guilyardi, and J. Cole, 2003: Simulation of the Madden–Julian oscillation in a coupled general circulation model. Part II: The role of the basic state. *J. Climate,* **16,** 365–382.

Jones, C., L. M. V. Carvalho, R. W. Higgins, D. E. Waliser, and J.-K. E. Schemm, 2004: Climatology of tropical intraseasonal convective anomalies: 1979–2002. *J. Climate,* **17,** 523–539.

Kanamitsu, M., W. Ebisuzaki, J. Woollen, S.-K. Yang, J. J. Hnilo, M. Fiorino, and G. L. Potter, 2002: NCEP–DOE AMIP-II Reanalysis (R-2). *Bull. Amer. Meteor. Soc.,* **83,** 1631–1643.

Kawamura, R., R. T. Murakami, and B. Wang, 1996: Tropical and midlatitude 45-day perturbations during the northern summer. *J. Meteor. Soc. Japan,* **74,** 867–890.

Kemball-Cook, S., and B. Wang, 2001: Equatorial waves and air–sea interaction in the boreal summer intraseasonal oscillation. *J. Climate,* **14,** 2923–2942.

——, ——, and X. Fu, 2002: Simulation of the intraseasonal oscillation in the ECHAM-4 model: Impact of coupling with an ocean model. *J. Atmos. Sci.,* **59,** 1433–1453.

Krishnamurti, T. N., D. K. Osterhof, and A. V. Mehta, 1988: Air-sea interaction on the time scale of 30 to 50 days. *J. Atmos. Sci.,* **45,** 1304–1322.

Krishnan, R., C. Zhang, and M. Sugi, 2000: Dynamics of breaks in the Indian summer monsoon. *J. Atmos. Sci.,* **57,** 1354–1372.

Lau, K.-M., and P. H. Chan, 1986: Aspects of the 40–50 day oscillation during the northern summer as inferred from the outgoing longwave radiation. *Mon. Wea. Rev.,* **114,** 1354–1367.

Lawrence, D. M., and P. J. Webster, 2001: Interannual variations of the intraseasonal oscillation in the South Asian summer monsoon region. *J. Climate,* **14,** 2910–2922.

——, and ——, 2002: The boreal summer intraseasonal oscillation: Relationship between northward and eastward movement of convection. *J. Atmos. Sci.,* **59,** 1593–1606.

Madden, R. A., and P. R. Julian, 1994: Observations of the 40–50-day tropical oscillation—A review. *Mon. Wea. Rev.,* **122,** 814–837.

Maloney, E. D., and D. L. Hartmann, 2000: Modulation of eastern North Pacific hurricanes by Madden–Julian oscillation. *J. Climate,* **13,** 1451–1460.

——, and J. T. Kiehl, 2002: MJO-related SST variations over the tropical eastern Pacific during Northern Hemisphere summer. *J. Climate,* **15,** 675–689.

Mo, K. C., 2000: Intraseasonal modulation of summer precipitation over North America. *Mon. Wea. Rev.,* **128,** 1490–1505.

North, G. R., T. L. Bell, R. F. Cahalan, and F. J. Moeng, 1982: Sampling errors in the estimation of empirical orthogonal functions. *Mon. Wea. Rev.,* **110,** 699–706.

Pacanowski, R. C., and S. M. Griffies, 1998: MOM 3.0 manual. NOAA/Geophysical Fluid Dynamics Laboratory, Princeton, 668 pp.

Pan, H.-L., and W.-S. Wu, 1995: Implementing a mass flux convection parameterization package for the NMC medium-range forecast model. NMC Office Note 409, 40 pp.

Reynolds, R. W., N. A. Rayner, T. M. Smith, D. C. Stokes, and W. Wang, 2002: An improved in situ and satellite SST analysis for climate. *J. Climate,* **15,** 1609–1625.

Saha, S., and Coauthors, 2006: The NCEP Climate Forecast System. *J. Climate,* **19,** 3483–3517.

Seo, K.-H., and K.-Y. Kim, 2003: Propagation and initiation mechanisms of the Madden-Julian oscillation. *J. Geophys. Res.,* **108,** 4384, doi:10.1029/2002JD002876.

——, and Y. Xue, 2005: MJO-related oceanic Kelvin waves and the ENSO cycle: A study with the NCEP Global Ocean Data Assimilation. *Geophys. Res. Lett.,* **32,** L07712, doi:10.1029/2005GL022511.

——, J.-K. Schemm, C. Jones, and S. Moorthi, 2005: Forecast skill of the tropical intraseasonal oscillation in the NCEP GFS dynamical extended range forecasts. *Climate Dyn.,* **25,** 265–284.

Shinoda, T., 2005: Impact of the diurnal cycle of solar radiation on intraseasonal SST variability in the western equatorial Pacific. *J. Climate,* **18,** 2628–2636.

——, H. H. Hendon, and J. Glick, 1998: Intraseasonal variability of surface fluxed and sea surface temperature in the tropical western Pacific and Indian Oceans. *J. Climate,* **11,** 1685–1702.

Sikka, D. R., and S. Gadgil, 1980: On the maximum cloud zone and the ITCZ over Indian longitudes during the south west monsoon. *Mon. Wea. Rev.,* **108,** 1840–1853.

Sperber, K. R., 2003: Propagation and the vertical structure of the Madden–Julian oscillation. *Mon. Wea. Rev.,* **131,** 3018–3037.

——, 2004: Madden–Julian variability in NCAR CAM2.0 and CCSM2.0. *Climate Dyn.,* **13,** 769–795.

Waliser, D. E., K. E. Lau, and J. H. Kim, 1999: The influence of coupled sea surface temperatures on the Madden–Julian Oscillation: A model perturbation experiment. *J. Atmos. Sci.,* **56,** 333–358.

Wang, B., and H. Rui, 1990: Dynamics of the coupled moist Kelvin–Rossby wave on an equatorial β-plane. *J. Atmos. Sci.,* **47,** 397–413.

——, and X. Xie, 1997: A model for the boreal summer intraseasonal oscillation. *J. Atmos. Sci.,* **54,** 72–86.

——, and ——, 1998: Coupled modes of the warm pool climate system. Part I: The role of the air–sea interaction in maintaining the Madden–Julian oscillation. *J. Climate,* **11,** 2116–2135.

Wang, W., S. Saha, H.-L. Pan, S. Nadiga, and G. White, 2005: Simulation of ENSO in the new NCEP Coupled Forecast System Model (CFS). *Mon. Wea. Rev.,* **133,** 1574–1593.

Wheeler, M., and H. H. Hendon, 2004: An all-season real-time multivariate MJO index: Development of an index for monitoring and prediction. *Mon. Wea. Rev.,* **132,** 1917–1932.

Woolnough, S. J., J. M. Slingo, and B. J. Hoskins, 2000: The relationship between convection and sea surface temperature on intraseasonal timescales. *J. Climate,* **13,** 2086–2104.

Xie, P., and P. A. Arkin, 1997: Global precipitation: A 17-year monthly analysis based on gauge observations, satellite estimates, and numerical model outputs. *Bull. Amer. Meteor. Soc.,* **78,** 2539–2558.

Zhang, C., 1996: Atmospheric intraseasonal variability at the surface in the tropical western Pacific Ocean. *J. Atmos. Sci.,* **53,** 739–758.

——, and M. Dong, 2004: Seasonality in the Madden–Julian oscillation. *J. Climate,* **17,** 3169–3180.

Zhang, M. H., and M. A. Geller, 1994: Selective excitation of tropical atmospheric waves in wave-CISK: Effect of vertical wind shear. *J. Atmos. Sci.,* **51,** 353–368.

Zheng, Y., D. E. Waliser, W. F. Stern, and C. Jones, 2004: The role of coupled sea surface temperatures in the simulation of the tropical intraseasonal oscillation. *J. Climate,* **17,** 4109–4134.